JOURNAL OF THERMOPHYSICS AND HEAT TRANSFER
Vol. 16, No. 1, January–March 2002

Modeling of Flow and Radiation in the Atlas Plume

A. A. Alexeenko,* N. E. Gimelshein,† and D. A. Levin‡
Pennsylvania State University, University Park, Pennsylvania 16802
R. J. Collins,§ R. Rao,¶ and G. V. Candler**
University of Minnesota, Minneapolis, Minnesota 55455
S. F. Gimelshein††
George Washington University, Washington, D.C. 20052
J. S. Hong‡‡ and T. Schilling§§
Institute for Defense Analyses, Alexandria, Virginia 22311

Modeling results and data are presented for a chemically reacting flow from a thrusting Atlas II rocket at low altitudes. High spatial resolution imagery and spectra have been obtained for a kerosene/liquid oxygen multinozzle plume at altitudes in the continuum flow regime. A numerical solution for a three-dimensional plume flow from the Atlas rocket engine is obtained using two different Navier–Stokes computational fluid dynamics codes. The influence of the flow near the rocket body on the plume structure is considered at an altitude of 40 km. The plume flowfields at 15- and 40-km altitudes are used for radiation calculations in the infrared spectral region. Calculated spectral radiant intensities and pixelated images are compared with the data extracted from the recent in-flight measurements. Comparison of the modeling with the data shows that numerical modeling is able to predict the plume structure existing at both altitudes. We find that it is necessary to include solid carbon particles as a radiating species to improve the agreement between simulated and measured radiation signatures.

Nomenclature

M = Mach number
p = pressure, Pa
T = temperature, K
u = velocity, m/s
θ = roll angle, deg
φ = aspect angle, deg
χ = mole fraction

Introduction

DURING the last decades rocket engine exhaust plumes have been a subject of intensive interdisciplinary study. Rocket exhaust plume phenomenology combines the gasdynamics of a chemically reacting mixture of gaseous and particulate species as well as the radiative transport of the nonhomogeneous emitting and scattering flowfield. A description of the major kinetic and optical processes in solid and liquid engine exhaust flows is given in Ref. 1. Despite the availability of thermochemical, excitation, and radiation models, the computationally intensive nature of flowfield modeling has made three-dimensional plume solutions difficult to obtain. To model numerically the continuum plume flowfield, two assumptions are frequently made. First, the flow at a given altitude is assumed to be steady, which is valid if motor transient effects on the plume can be ignored. This has been assumed to be the case in the work reported here. The second, more significant, assumption commonly made is that of a single equivalent nozzle, that is, the plume is considered to be axisymmetric and equivalent in terms of the mass flow rate to a three-dimensional multinozzle plume. Earlier work showed that the simplifying assumption of the single equivalent nozzle is not adequate to resolve the multinozzle plume structure observed in the rocket plume radiance images taken at different altitudes.[2]

The experimental study of rocket engine plumes has been carried out since the late 1950s, and databases of observations of missile launches have been created from the measurements of plume radiation signatures from satellite-, aircraft-, and ground-based sensors.[3] Within the last five years, the Innovative Science and Technology Experimentation Facility (ISTEF) has developed a unique capability to collect multiband, high spatial resolution, calibrated imagery of rocket engine exhaust plumes in-flight from ground-based focal plane array systems.[4] Of particular interest are the recent measurements in mid-wavelength infrared (MWIR) and UV spectral region that have been taken of an Atlas II kerosene/liquid oxygen (LOX) engine exhaust plume. The images provide detailed shock structure of the plume from the liftoff up to an altitude of approximately 100 km. The ISTEF data show dramatic changes in the multinozzle plume structure as the Atlas rocket ascends.

To explain the major plume phenomenology captured in the radiance images from the Atlas flight, two representative altitude conditions were selected, 15 and 40 km. The images at these altitudes show distinctive plume structures for moderately and highly underexpanded flows. The difference in ambient pressures affects the relative importance of different kinetic processes at these two altitudes. Typically, at low altitudes (10–15 km), the fuel afterburning process is the leading mechanism, whereas, at higher altitudes (30–50 km), the process of mixing dominates the formation of the plume

Received 19 April 2001; revision received 18 August 2001; accepted for publication 20 September 2001.

*Graduate Assistant, Aerospace Engineering Department, 233 Hammond Building; alexeenko@psu.edu. Student Member AIAA.
†Graduate Assistant, Aerospace Engineering Department, 233 Hammond Building; ngimel@psu.edu.
‡Associate Professor, Aerospace Engineering Department, 233 Hammond Building; dalevin@psu.edu. Senior Member AIAA.
§Professor Emeritus, Electrical and Computer Engineering Department, 200 Union Street S.E.; swbemac@aol.com. Senior Member AIAA.
¶Research Associate, Department of Aerospace Engineering and Mechanics, 107 Akerman Hall, 110 Union Street; S.E.; rao@aem.umn.edu.
**Professor, Department of Aerospace Engineering and Mechanics, 107 Akerman Hall, 110 Union Street S.E.; candler@aem.umn.edu. Senior Member AIAA.
††Senior Research Scientist, Chemistry Department, 7252 1st Street N.W.; gimel@gwu.edu. Member AIAA.
‡‡Research Staff Member, Systems Evaluation Division, 1801 N. Beauregard Street.
§§Research Staff Member, Science and Technology Division, 1801 N. Beauregard Street.

structure. In Refs. 2 and 5, the first fully coupled chemically reacting, three-dimensional, multinozzle flows were numerically modeled at 15- and 40-km altitudes.

The previous Atlas plume modeling efforts emphasized the jet–atmospheric interaction.[2] Several issues were addressed to improve the fidelity of the flow solutions such as grid resolution and turbulence modeling.[5] A numerical study[6] of various modeling issues has been conducted recently for the Titan twin-nozzle engine flow, and the significant influence of the rocket body on the plume flowfield was shown. An important objective of this work is to include the vehicle–plume interaction in the computational fluid dynamics (CFD) modeling of multinozzle plume flow, to study its influence on the simulated imagery and to compare the results of computations with the available experimental data.

The numerical solution of the flow around a three-dimensional model of the Atlas rocket at an altitude of 40 km is obtained with a Navier–Stokes code, GASP,[7] and the impact of the bow-shock and boundary layer on the plume structure and radiation is examined. The numerical solutions for 15- and 40-km altitudes are used as input to the radiation calculations to predict the plume spatial radiation distribution in the IR and UV spectral regions.[8] Both molecular radiation from gaseous species and continuum radiation from plume particulates are considered. Carbon soot particles are assumed to be present in the plume at a constant mass fraction and to follow the gas flow along the streamlines. To compare the calculations with field data, the effect of the atmospheric transmission and the viewing geometry between the plume and the ground observation site must be considered. The MODTRAN atmospheric model[8] was used to estimate the wavelength specific attenuation of the plume radiance. The best estimated trajectory was used to calculate the vehicle altitude, slant range, and aspect and roll angles. At higher altitudes, the vehicle aspect angle is significantly different from that of a crossing geometry. The results of the radiation imagery and spectral calculations are compared with in-flight data in the MWIR spectral region. The combined CFD and radiation modeling results show good agreement with the experimental data.

CFD Method

The numerical solution of the Navier–Stokes equations for a chemically reacting gas flow has been obtained with finite volume spatial discretization on a structured three-dimensional grid implemented in GASP. The solution was generated for the conditions of 40 km. Laminar flow is assumed in these computations, and viscous derivative terms in the momentum conservation equation are computed with second-order accuracy in the interior and gas–solid surface interface cells. The Van Leer flux vector splitting was used for the convective fluxes. The third-order upwind-biased scheme is applied for the spatial reconstruction of volume properties in the cell boundaries. To obtain a steady-state solution, two-factor approximate factorization is used for time stepping. For the 15-km conditions, the CFD solutions from Ref. 9 were used. A similar code was used to obtain the solution, except that the effect of the hard body was neglected. A k–ϵ turbulence model was included to model the effects of turbulence.

The vehicle geometry used in the computations consists of an axisymmetric front part representing the forward solid-body flow and a three-dimensional aft part representing the aft solid body and plume flowfield. Geometric parameters for the model were taken from Ref. 10. With the origin at the center of symmetry of the multinozzle exit plane, the computational domain was chosen to be 46.2 m upstream and 150 m downstream. The computational grid consists of three regions, as is shown in Fig. 1. (Note that grid 3 is partially shown.) The first grid (closest to the nose) is used to model the flow over the axisymmetric part of the vehicle. In the next two regions, the aft body and the multinozzle plume, the grid is three dimensional. The grid for the axisymmetric part has two zones, each with 100×60 and $130 \times$ cells. The aft body grid has $120 \times 140 \times 65$ cells, and the plume zone has $150 \times 140 \times 65$ cells. A grid consisting of a total of 2,470,800 cells were used. The computational grid at the exit plane $X = 0$ is shown in Fig. 2.

Table 1 Flow conditions

	Velocity, m/s	Pressure, Pa	Temperature, K
Freestream, km			
15	535	12,045	217
40	1,476	278	251
Nozzle,			
Atlas booster	2,930	78,410	2,380
Atlas sustainer	3,280	20,200	1,684

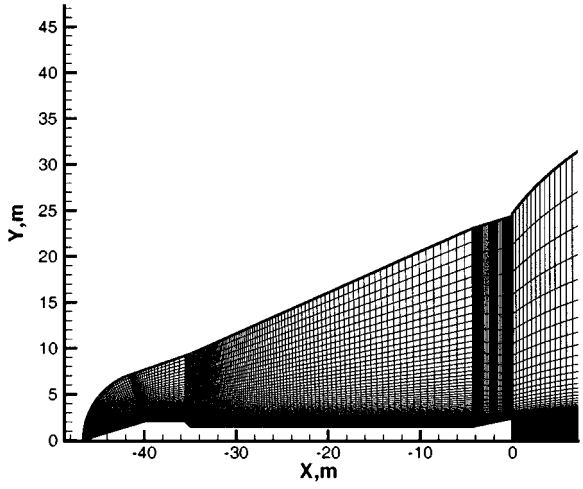

Fig. 1 Computational grid in *XY* plane.

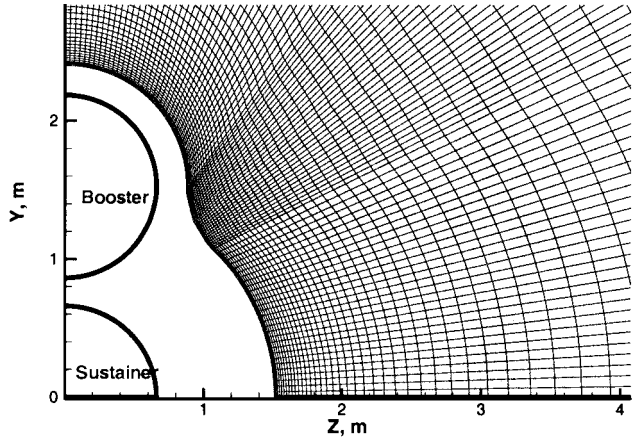

Fig. 2 Computational grid at the exit plane $X = 0$.

The grid resolution issues for an Atlas plume flow at 40 km have been discussed previously in Refs. 2 and 11. At present, a rigorous grid convergence study for three-dimensional plume modeling is not feasible, and, therefore, the numerical solutions used in this work may not meet the traditional grid resolution criteria. Nevertheless, an a posteriori analysis of the solution and radiance measurements shows good agreement in the spatial distribution of the plume structure.

Inflow conditions at the nozzle exit plane and freestream ambient conditions at 15 and 40 km are summarized in Tables 1 and 2. At the gas–solid surface interface a no-slip condition with adiabatic temperature is used. Standard two-way ghost cell mapping is employed at the zonal boundaries. At the outflow boundary, 150 m downstream of the nozzle exit plane, a second-order extrapolation is applied. The 15-km calculations use a similar flux vector splitting method and implicit time integration. They include a two-equation turbulence model, but ignore the effects of the hard body on the plume flow (see Refs. 5 and 9 for more details).

The exhaust gases from the Atlas kerosene/LOX motor consist primarily of H_2O, CO, CO_2, and H_2. Because of the high temperature

Table 2 Mole fractions of chemical species

Species	Freestream	Atlas booster	Atlas sustainer
H_2	0.00000	0.11849	0.17706
O_2	0.21017	0.00013	0.00000
H_2O	0.00000	0.37160	0.31970
H	0.00000	0.00564	0.00012
O	0.00000	0.00010	0.00000
OH	0.00000	0.00325	0.00001
N_2	0.78953	0.00000	0.00000
CO	0.00000	0.32488	0.32643
CO_2	0.00030	0.17591	0.17669

at the nozzle exit and the shear layer, chemical reactions occur in the gaseous mixture and affect the optical radiation. Including the freestream gases N_2, O_2, and CO_2 and the reaction products, a nine-species mixture is used in the flow calculations. The following set of five exchange and five recombination reactions has been used in the calculations:[2]

$$\mathrm{OH + H_2 \leftrightarrow H_2O + H}, \qquad \mathrm{OH + OH \leftrightarrow H_2O + O}$$

$$\mathrm{OH + O \leftrightarrow H + O_2}, \qquad \mathrm{O + H_2 \leftrightarrow OH + H}$$

$$\mathrm{H + H + M \leftrightarrow H_2 + M}, \qquad \mathrm{H + O + M \leftrightarrow OH + M}$$

$$\mathrm{H + OH + M \leftrightarrow H_2O + M}, \qquad \mathrm{O + O + M \leftrightarrow O_2 + M}$$

$$\mathrm{CO + OH \leftrightarrow CO_2 + H}, \qquad \mathrm{CO + O + M \leftrightarrow CO_2 + M}$$

where M can be any of the chemical species.

Radiation Calculations

The Standard Infrared Radiation Model (SIRRM) and SPURC[3,8] have been used to calculate the spectral and spatial distribution of the plume radiation in the IR spectral region. The CFD solutions for the Atlas plume flowfields at 15 and 40 km have been used to provide the species concentrations, pressures, and temperatures as a function of location in the plume as is required to calculate the radiation. The two programs use a general radiative transfer formalism to model the emission lines from gaseous molecular species and the continuum emission from solid particulate species. Absorption and scattering due to plume gaseous and particulate species are modeled as well. To compare calculations with experimental data, the plume source radiance must be attenuated by the atmospheric extinction. The moderate bandwidth resolution atmospheric model, MODTRAN, was used.[3,8]

An important input parameter for the radiation calculations is the location of the observer with respect to the plume. The viewing geometry for the case of a three-dimensional plume flowfield is given by the rocket altitude and the aspect and roll angles. The aspect angle φ is the angle between the vector defined by the line of sight from the ground-based instruments to the rocket and the rocket's velocity vector. The roll angle θ is the azimuthal angle between the projection of the line-of-sight vector onto the nozzle exit plane and the axis along which the three nozzles are aligned (Fig. 3). The viewing geometry was calculated from the best estimated trajectory for the various missions. Comparison with postflight trajectories did not show appreciable differences for the two missions considered.

Results and Discussion

Rocket and Plume Flowfields at 40 Kilometers

First, the influence of the vehicle–plume interaction on the flow structure is considered. The vehicle Mach number at 40-km altitude is equal to 4.7, and the bow shock is relatively strong. Figure 4 shows the calculated Mach number and temperature contours near the vehicle. The boundary layer near the vehicle surface affects the expansion of propellant gases from the rocket multinozzle.

The influence of the vehicle on the plume structure is illustrated by temperature contours in crossplanes at 1 and 40 m downstream

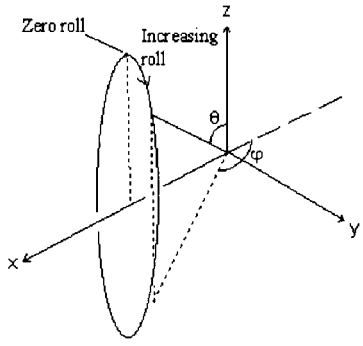

Fig. 3 Definition of aspect angle φ and roll angle θ

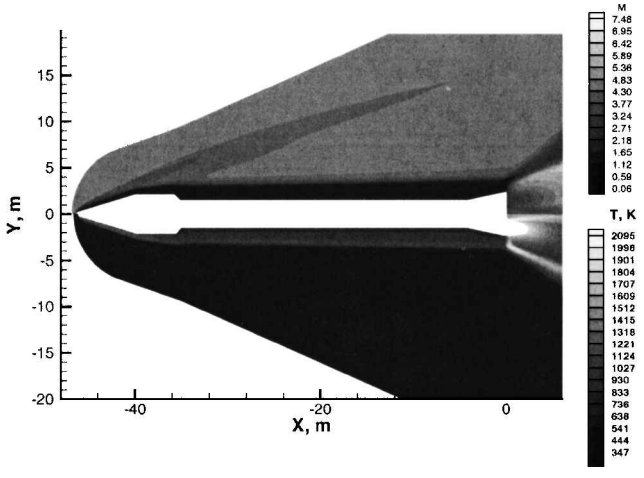

Fig. 4 Mach number (top) and temperature (bottom) contours in the symmetry plane $z = 0$ m for Atlas at 40 km.

from the nozzle exit plane, as shown in Fig. 5. It is seen that the subsonic boundary layer near the vehicle affects both the near-field and far-field structure of the plume. The temperature contours in the symmetry plane at $z = 0$ are plotted in Fig. 6 for the flow solutions with and without the solid body. Figure 7 provides an expanded view of the detailed flow structure. There is a significant quantitative difference between the two solutions. In particular, the temperature in the shear layer is significantly lower with the body-induced plume backflow, and the barrel shock reflection is located 20 m closer to the multinozzle exit plane.

Now let us consider the spatial distribution of chemical species, which are important in the radiation modeling. Figure 8 shows contour levels of the mole fraction of CO in the plume with and without the body. In both calculations, the concentration of CO, a major propellant species, is seen to be reduced in the shear layer only. There is little change in the chemical composition in the core of the plume, where chemical reactions are slow compared to the gas residence time. In the shear layer, however, the gas temperatures are relatively high, and the gases move more slowly. The CO concentration in the shear layer is reduced by the last reaction given at the end of the "CFD Method" section. Figure 8 shows that the inclusion of the body influences the CO concentration in the shear layer because the gas temperatures and shear layer structure are different in the two cases. Again, the presence of the body thickens the shear layer and, therefore, increases the region where chemical reactions are important.

In addition to CO, water, carbon dioxide, and OH are chemical species that also contribute to the IR and UV plume radiance. Figure 9 shows a comparison of the carbon dioxide and water mole fractions at 40 km with the rocket body. The water mole fraction distribution decreases in the mixing layer and high-temperature region of the plume core structure. Water dissociates in the shear layer to form OH, a strong UV emitter by the reverse of the second chemical reaction given earlier. Because OH is only present in the nozzle exit at very low concentrations, a significant amount of it will exist

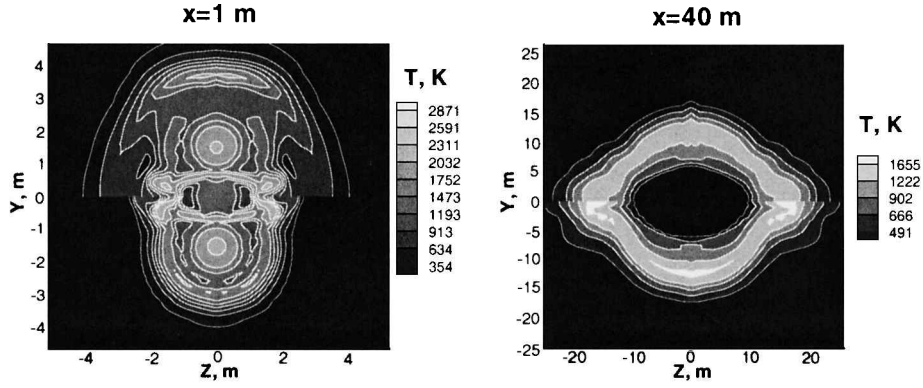

Fig. 5 Temperature contours in the crossplanes $x = 1$ and 40 m for Atlas rocket plume at 40 km (upper part, with rocket body, and bottom part, without body).

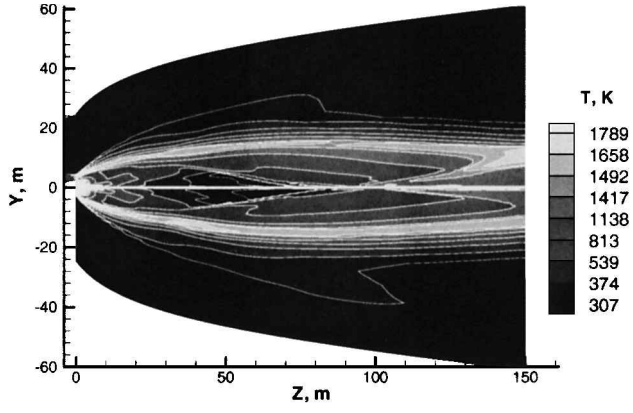

Fig. 6 Temperature contours for an Atlas rocket plume at 40 km (upper part, with rocket body, and bottom part, without body).

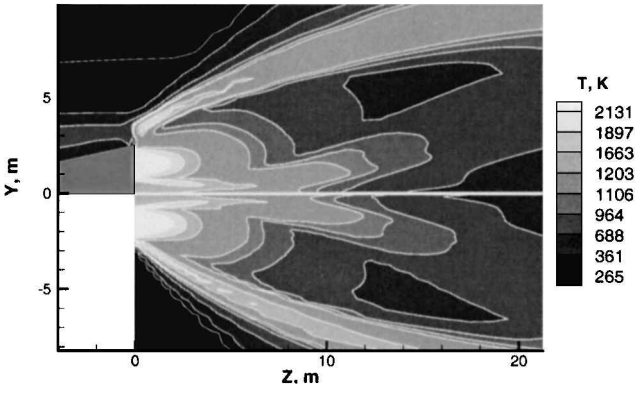

Fig. 7 Expanded view of region close to the nozzle of temperature contours for an Atlas rocket plume at 40 km (upper part, with rocket body and bottom part, without body).

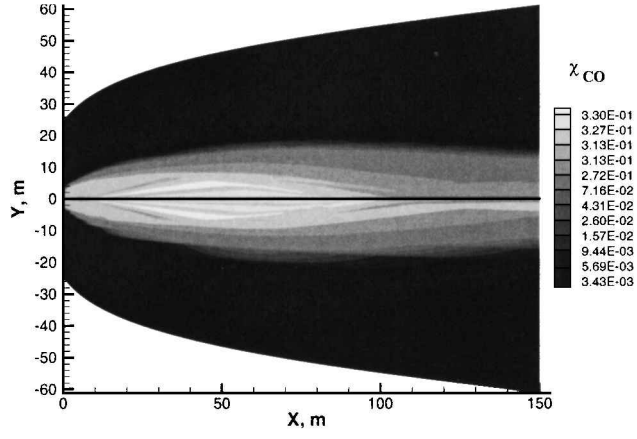

Fig. 8 CO mole fraction contours at 40 km, with (top) and without (bottom) the rocket body.

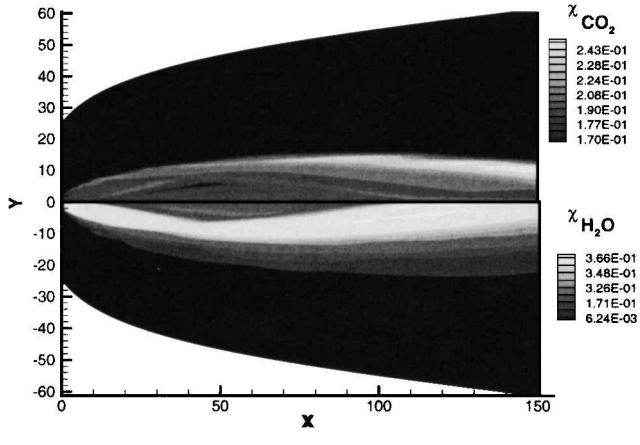

Fig. 9 CO_2 (top) and water (bottom) mole fraction contours at 40 km, with the rocket body.

only in the shear layer. Carbon dioxide is also present as an exhaust species, but is approximately 50% lower in concentration than water or CO. Unlike water, the carbon dioxide concentration can increase and decrease due to the last reaction shown earlier proceeding in both the forward and reverse directions. The relative emphasis of either direction will depend on the local gas temperature and the relative concentrations of CO, O, and third body species. The CO_2 concentration increases in the shear layer, where the plume mixes with the ambient gas.

Plume Radiance

With steady-state spatial distributions of temperature and species concentrations plume radiation can be modeled. This paper concentrates on the MWIR radiance, and available UV data will be presented in future work. To compare with the data, the MWIR radiation from the plume at 15 and 40 km has been analyzed in terms of spectral radiance intensity and radiance images averaged over the pixel size of the imagery data.

Figures 10 and 11 show the calculated spectra for 15- and 40-km altitude, respectively, for a crossing geometry ($\varphi = 90$ deg and $\theta = 90$ deg). The spectra are spatially integrated over the plume area. Figures 10 and 11 show spectra calculated assuming the presence of molecular radiation only (designated as no-soot) and molecular plus soot-continuum radiation. Consider first the molecular radiation that is calculated directly from the flow modeled molecular species

concentrations (no-soot). The molecular spectra in the MWIR spectral region exhibits two main peaks. The first one at 2.7–2.8 μm corresponds to the H_2O fundamental and CO_2 combination bands, whereas the second one, at 4.3–4.6 μm, is due to radiation from the CO_2 fundamental band.[12] Note that the ratio of the radiant intensity for the two peaks is different for the 15- and 40-km altitude spectra. The radiant intensity is higher in the 2.7-μm band than at 4.3 μm at 15 km, but lower at 40 km. The main reason for the peak reversal is due to the greater local absorption in the plume within the 4.3–4.6 μm band, which is more significant at lower altitudes. To a first approximation, the absorption coefficient varies linearly with pressure, and the ambient pressure to which the plume equilibrates to is about 50 times higher at 15- than at 40-km altitude (see Table 1). Therefore, the optical thickness of the plume is greater at 15 than at 40 km. Because of to plume optical thickness, the change in plume spectral radiant intensity from 15 to 40 km cannot be attributed to changes in the relative importance of the chemical reactions given earlier.

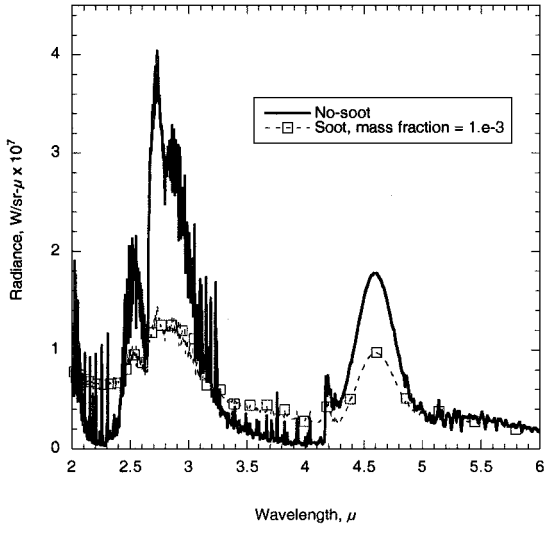

Fig. 10 Calculated spectral radiant intensity at 15 km, $\varphi = 90$ deg, and $\theta = 90$ deg.

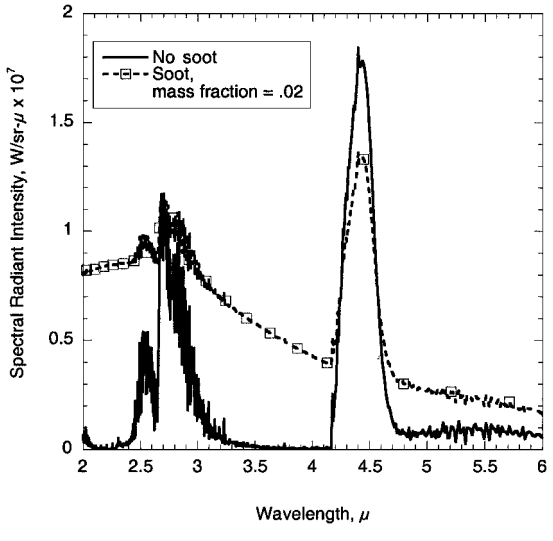

Fig. 11 Calculated spectral radiant intensity at 40 km, $\varphi = 90$ deg, and $\theta = 90$ deg.

The spectral radiant intensity calculated with a constant mass fraction of carbon particles is also plotted in Figs. 10 and 11 for 15 and 40 km, respectively. The soot–carbon particles are formed due to incomplete combustion and can significantly affect the spectra. The soot is modeled as 20-nm radius spherical particles present at a constant mass fraction. It is assumed that the carbon particles are in thermal equilibrium with the gas flow and follow the gas streamlines. A lower mass fraction of soot is assumed at 15 km, because soot oxidation (not modeled in this work) would reduce the soot concentration relative to that at 40 km. The presence of soot at each altitude increases the background between the molecular peaks due to scattering. The soot particles decrease the radiant intensity within the peaks of molecular radiation due to absorption.

Now we consider the isoradiance contours obtained from the flowfield solutions. Images will be simulated for the molecular and soot bandpasses, 4.667–4.802 and 3.673–3.787 μm, respectively. Figure 12 shows the isoradiance contours for the flowfield with and without the body for no-soot at 40 km, at a crossing geometry. Over a large spatial scale, the difference in the two radiation contour plots does not appear to be significant. Note, however, that the flow recompression occurs earlier with the body geometry included, resulting in an increased radiance signal at approximately 100 m from the nozzle exit. Also, for the region of flow near the exit plane (Fig. 13), the radiance patterns are different.

To compare the simulated image with the data it is necessary to integrate the radiance over line of sights through the plume that correspond to the viewing geometry. The plume aspect angle is readily obtained from preflight or postflight rocket trajectory data. The orientation of the three nozzles relative to the plume–rocket axis (roll-angle) can only be estimated from the same data. Figure 14 shows the sensitivity of the radiance contours in the molecular bandpass of 4.667–4.802 μm, for the flowfield solutions that do not include the body and the no-soot case. (Examination of Fig. 11 shows that molecular radiation dominates in this spectral bandpass.) As the nozzles are rotated from 0 to 90 deg, the axial symmetry apparent in the 0 deg simulated image is reduced and then regained at 90 deg. At 0 deg, the three nozzles are stacked one on top of the other, and at 90 deg they are lined up one behind the other. From comparison with the flight data, we have derived a roll angle close to 60 deg. Hence, we could expect to see a similar asymmetry in the field image data as well.

Figure 15 shows a comparison of the isoradiance contours at the experimental viewing geometry calculated with and without the rocket body at 40 km. Differences can be observed in the radiance structure both near and far from the nozzle exit. Note, however, that the flowfield computed with the rocket body tends to enhance the secondary plume structure observed approximately 75 m from the nozzle exit. Note that the plume is foreshortened due to the

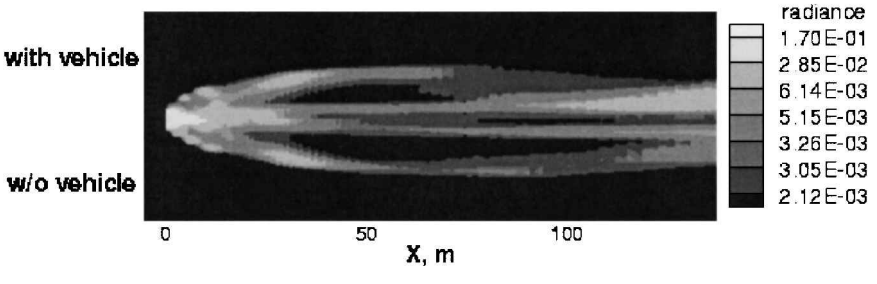

Fig. 12 Comparison of the calculated source radiance (W/sr · cm^2) in the 4.667–4.802 μm spectral band at 40 km for the flow solution with and without the body at $\varphi = 90$ deg and $\theta = 90$ deg.

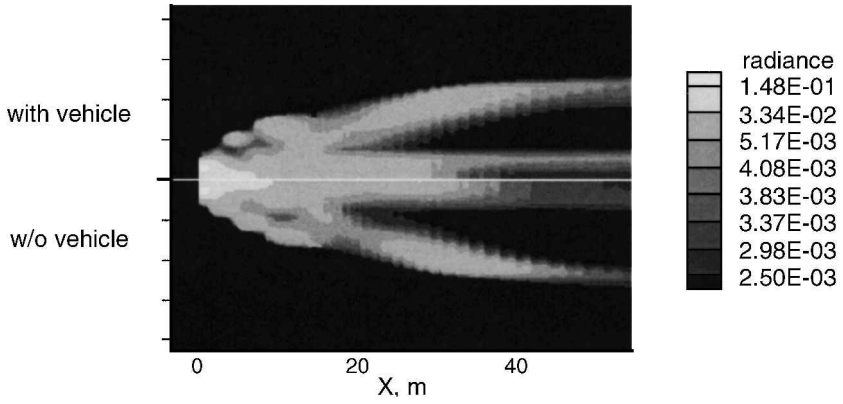

Fig. 13 Comparison of the calculated source radiance (W/sr · cm^2) in the 4.667–4.802 μm spectral band at 40 km for the flow solution with and without the body at $\varphi = 90$ deg and $\theta = 90$ deg. Note in this plot and others that follow, the *y* axis is the same scale as the *x* axis.

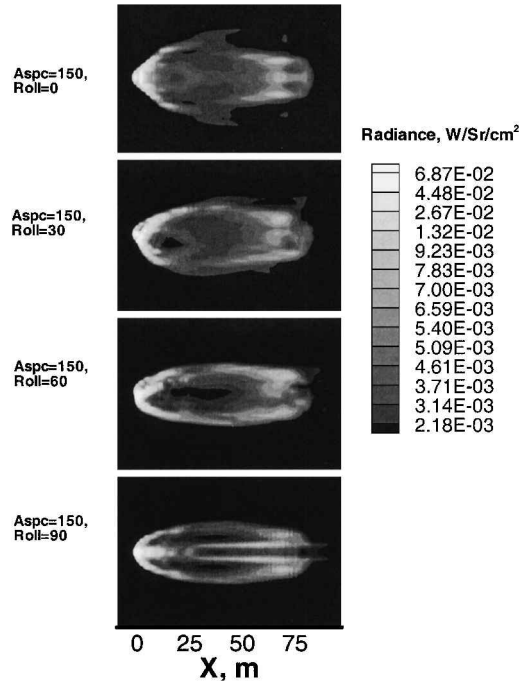

Fig. 14 Calculated source radiance in the 4.667–4.802 μm spectral band at 40 km for different viewing geometries.

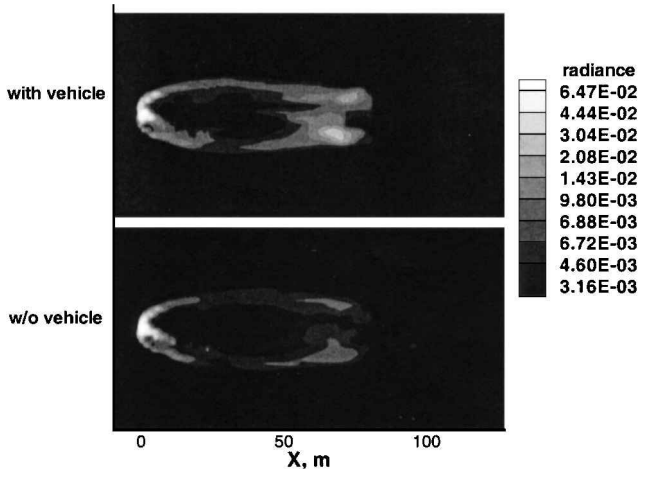

Fig. 15 Calculated source radiance (W/sr · cm^2) in the 4.667–4.802 μm spectral band at 40 km for $\varphi = 150$ deg and $\theta = 60$ deg for the flow solution with (top) and without (bottom) the rocket body.

high aspect angle of the viewing geometry. The increase in far-field radiance is a result of the stronger compression due to the influence of the hard body (see Fig. 12).

Comparison with Field Data

MWIR imagery data were obtained with a mid-IR amber focal planar array (FPA) system equipped with a filter wheel with a variety of bandpass and neutral density filters. The IR array contains 256×256 pixel elements. A major experimental goal was to control the dynamic range of the arrays so that the plume radiance data would be unsaturated where ever possible. The FPA systems were calibrated with extended- and cavity-type blackbody sources. Additional details of the calibration procedure are given elsewhere.[4] Typical calibrations provide radiance errors of 15%, which is much smaller than modeling uncertainties. Imagery have been obtained on liquid Atlas launches (without solid aluminized strap-on motors) for a variety of launches. Figures 16–19 show examples of MWIR imagery data and calculations in the 3.673–3.787 μm bandpass from the A7050 mission of May 1998 and the GOES-L mission of May 2000. In general, images from these missions show the same variation in the flow structure, with altitude. The range of radiance values are similar for the two missions, noting that atmospheric effects may not be identical. Figures 16 and 18 show that at an altitude of approximately 15 km, an apparent braided structure is seen. By 40-km altitude, the braided structure is replaced by a pitchfork structure, as can be seen in Figs. 17 and 19. Note that the apparent shortening of the plume in the images is an indication of the high (tail) aspect viewing angle.

By the use of the radiation modeling discussed, Fig. 18 shows a comparison of the simulated images at 15 km with and without soot with data. The braided structure of the plume that is seen at 15-km altitudes can only be captured with numerical modeling that takes into account multinozzle effects. The evolution in the plume structure from 15 to 40 km altitude is also predicted accurately by the three-dimensional flowfield calculations. At the higher altitude, Fig. 19 provides a comparison of the simulated images with and without soot with the data at 40 km. The inclusion of soot at a mass fraction of 2% in the radiation calculations dramatically changes the simulated image and is necessary to predict any of the plume structure seen in the imagery data. The calculation with 2% soot shows a secondary plume structure located 50 m from the nozzle. The calculations also adequately capture the asymmetry close to the nozzle exit observed in the data. An asymmetry in the secondary structure of the pitchfork is observed for both sets of data at 40 km, but is absent from the calculations. Two possible reasons account for this deficiency in the modeling. The radiation computational domain is constrained by that of the flow modeling, which extends out to only 150 m from the nozzle exit. Because of the high aspect viewing angle, there are contributions from the plume radiation at distances greater than 150 m from the nozzle, which are not included in the present calculations. If these contributions were included, we would

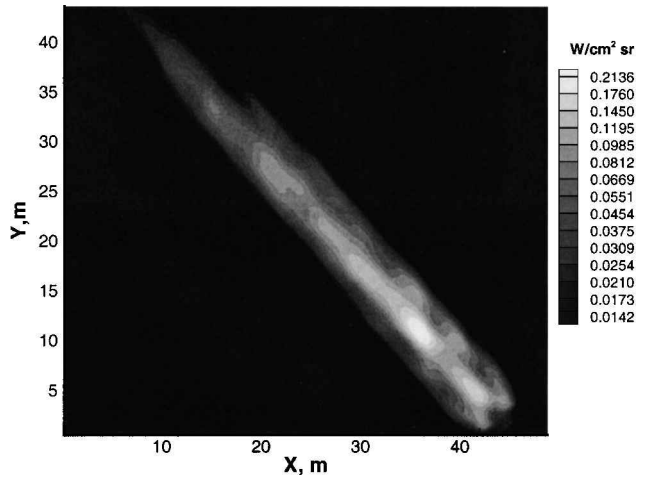

Fig. 16 Image from the A7050 mission of an Atlas in flight at 15-km altitude in the spectral bandpass of 3.673–3.787 μm; nozzle exit plane located in the lower right-hand corner.

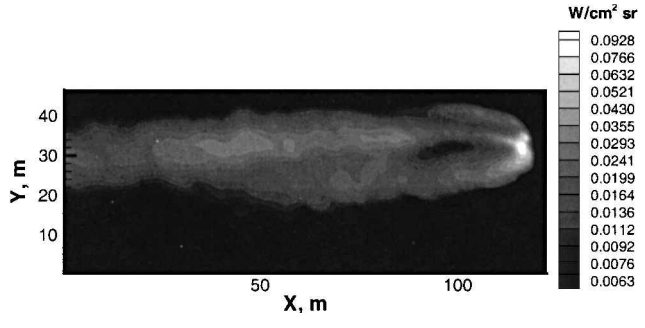

Fig. 17 Image from the A7050 mission of an Atlas in flight at 37-km altitude in the spectral bandpass of 3.673–3.787 μm.

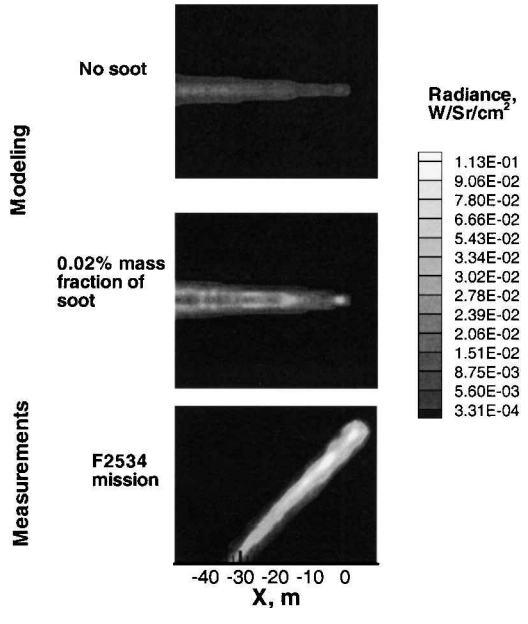

Fig. 18 Comparison of an image from the GOES-L (F2534) mission of an Atlas in flight at 15-km altitude in the spectral bandpass of 3.673–3.787 μm with calculations of apparent radiance with and without soot and for $\varphi = 120$ deg and $\theta = 90$ deg; nozzle exit plane located in the upper right-hand corner of the experimental image.

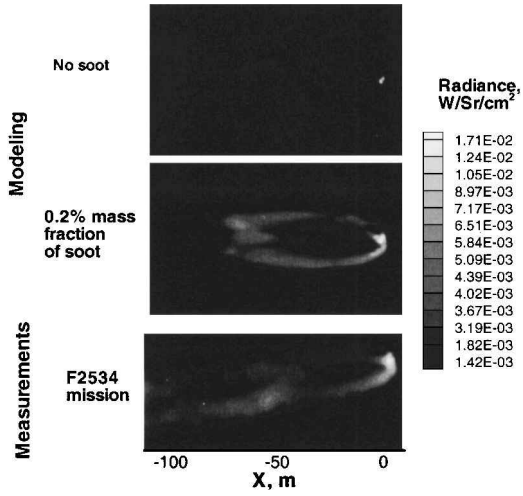

Fig. 19 Comparison of an image from the GOES-L (F2534) mission of an Atlas in flight at 40 km altitude in the spectral band pass of 3.673–3.787 μm with calculations of apparent radiance with and without soot and for $\varphi = 150$ deg; $\theta = 60$ deg for the flow with the rocket body.

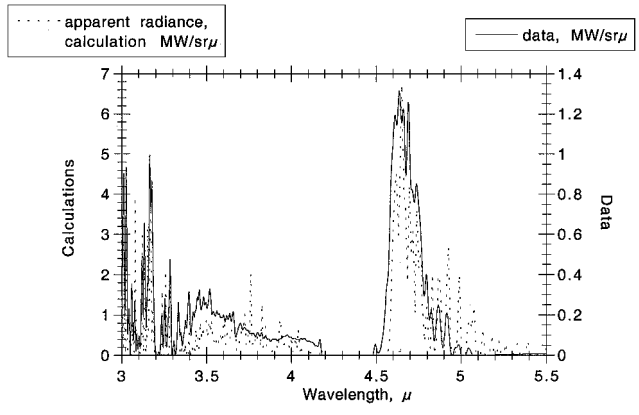

Fig. 20 Comparison of FTIR MWIR spectra and calculations for 15 km.

expect an asymmetry in the calculated image (for structure 50 m from the nozzle) to be similar to that obtained close to the nozzle seen in the data. A second possible contribution to the downstream asymmetry is due the presence of a gas generator for the Atlas II rocket system. This generator, which also produces soot, has not been modeled in the present calculations.

Finally, we consider the agreement between modeling and spectral data. MWIR spectral data were obtained from a recent Atlas observation by researchers from Arnold Engineering Development Center[4] working in conjunction with ISTEF. Data from approximately 3.0–5.50 μm were acquired using a Midac M204 Fourier transform spectrometer equipped with a liquid nitrogen cooled InSb detector. The spectrometer optics consisted of a 250-mm-diam f\4 Newtonian telescope that provided a 0.25-deg circular field of view. MWIR spectra were acquired at a rate of 5 scans per second with a spectral resolution of 8 cm^{-1}. Both spectrometers were calibrated in situ in units of irradiance using National Institute of Standards and Technology traceable sources.[4] Spectra were simulated at the experimental viewing geometry and spectral resolution of the Fourier transform IR at 15 and 40 km. Figures 20–22 show a comparison of the simulated apparent spectra with data at 15- and 40-km altitude. There is good agreement between the simulations and measurements for both altitudes. At 15 km, the mass fraction of soot used in the radiation calculation is sufficiently small such that the calculated apparent spectra are very similar. Examination of Figs. 21 and 22, at 40 km, shows that radiation calculation that includes soot agrees more closely with the measured spectra. The agreement

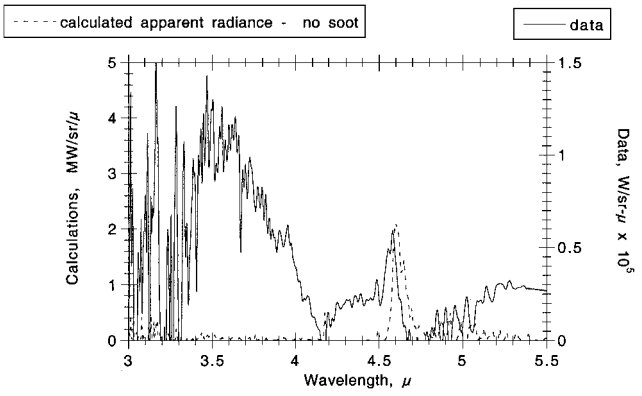

Fig. 21 Comparison of FTIR MWIR spectra and calculations without soot for 40 km.

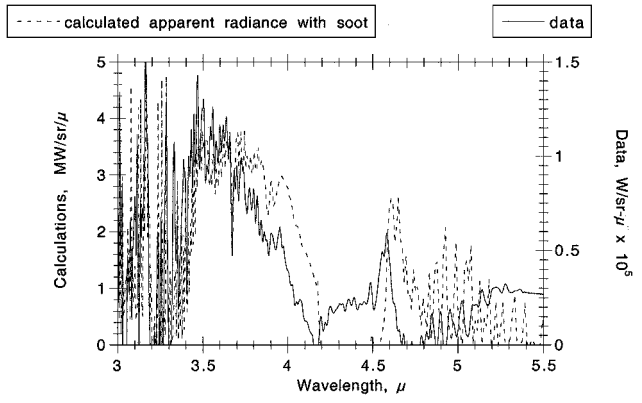

Fig. 22 Comparison of FTIR MWIR spectra and calculations for 40 km.

between simulated spectra with soot and data is poorer at wavelengths longer than 4.2 μm, probably due to the uncertainty in the actual amount of soot that affects the degree of absorption of molecular radiation.

Conclusions

CFD Navier–Stokes solutions for the Atlas multinozzle flow with finite-rate chemical reactions, at 15 and 40 km were obtained. The goal of the 15-km numerical study was to obtain a three-dimensional solution that could adequately account for multinozzle effects. The three-dimensional numerical solution at 40 km was obtained to study the influence of the vehicle on the plume flow structure. It is shown that the subsonic boundary layer near the vehicle affects both the near-field and far-field portions of the plume. With the inclusion of the vehicle–plume interaction, it was found that the temperature in the shear layer is significantly lower and the barrel shock reflection point is located 20 m closer to the nozzle exit plane.

Radiation calculations have been conducted for the Atlas plume at the two altitudes of 15 and 40 km. Plume imagery from various Atlas II missions show that at these altitudes the plume flow exhibits two distinct structures. The two altitudes qualitatively represent low- and high-altitude regions, where the rocket body plume flow can be modeled with continuum methods. The MWIR spectra are calculated as well as the pixelated images for the bandpass of the fielded detector arrays. The modeled spectra were found to be sensitive to the inclusion of soot, generally raising the background level of the molecular radiation, at both altitudes. The modeled images were also found to be sensitive to viewing geometry and the inclusion of soot at 15 and 40 km. The spatial distribution of the plume near-field radiation was found to be affected by the rocket body flow–plume interaction.

The calculated radiance images and spectra were compared with field data measurements. Comparison of simulated and measured images showed that modeling captures the significant change in the plume flowfield structure from 15 to 40 km. The comparisons also showed that it is necessary to include a finite amount of soot at both altitudes. Future work will consider soot oxidation, expected to be important at 15 km, to determine the variable soot mass fraction in the plume. Finally, the agreement between the magnitude of the measured and simulated image radiation is reasonably good. Comparison of measured and calculated spectra at both 15 and 40 km show good agreement in shape and magnitude. Again, the spectral comparison emphasizes the importance of including soot as a plume radiator.

Acknowledgments

The work at Pennsylvania State University and George Washington University was supported by the Space and Naval Warfare Systems Center San Diego Grant DUNS:04-399-0498 and Army Research Office Grant DAAG55-98-1-009 and at University of Minnesota by the Army Research Office Grant DA/DAAG55-97-1-0406. Computer time was provided by the University of Minnesota Supercomputer Institute. This work is also sponsored in part by the Army High Performance Computing Research Center under the auspices of the Department of the Army, Army Research Laboratory cooperative agreement DAAH04-95-2-0003/Contract DAAH04-95-C0008. This effort has involved the participation of additional investigators and years of effort in operations and mission planning at Innovative Science and Technology Experimental Facility. The joint effort of modelers and experimentalists provide a unique study of a highly complex flow. The Science and Technology Directorate of the Ballistic Missile Defense Organization is conducting programs to characterize and measure the UV and infrared radiation of rocket plumes with high spatial resolution.

References

[1]Vitkin, E. I., Karelin, V. G., Kirilin, A. A., Suprin, A. S., and Khadyka, J. V., "A Physico–Mathematical Model of Rocket Exhaust Plumes," *International Journal of Heat and Mass Transfer*, Vol. 40, No. 5, 1997, pp. 1227–1241.

[2]Hong, J. S., Levin, D. A., Collins, R. J., Emery, J., and Tietjen, A., "Comparison of Atlas Ground-Based Plume Imagery with Chemically Reacting Flow," AIAA Paper 97-2537, June 1997.

[3]Simmons, F. S., *Rocket Exhaust Plume Phenomenology*, Aerospace Press, EI Segundo, CA, 2000.

[4]Barton, P., Pearce, B., Freeman, N., Tietjen, A., Emery, J., Dawson, D., Wendt, J., Moyers, R., Hiers, R., and Lovern, M., "Atlas Spectral Imagery Data and Mechanisms," AIAA Paper 2001-1121, Jan. 2001.

[5]Rao, R. M., Sinha, K., Candler, G. V., Wright, M. J., and Levin, D. A., "Numerical Simulation of Atlas II Rocket Motor Plumes," AIAA Paper 99-2258, June 1999.

[6]Ebrahimi, H. B., Levine, J. L., and Kawasaki, A., "Numerical Investigation of Twin-Nozzle Rocket Plume Phenomenology," *Journal of Propulsion and Power*, Vol. 16, No. 2, 2000, pp. 178–186.

[7]GASP Ver. 3, The General Aerodynamic Simulation Program, Computational Flow Analysis Software for the Scientist and Engineer, User's Manual, Aerosoft Co., Blacksburg, VA, May 1996.

[8]Cox, J. W., Calia, V., Slack, M., Grillo, A., Konopka, W., Ryan, W., Leng, J., Green, B., Upschutte, B., and Holtclaw, K., "Standard Plume Ultraviolet Code (SPURC)," Phillips Lab., Rept. PL-TR-91-3004, Edwards AFB, CA, Jan. 1991.

[9]Candler, G., Rao, R., Sinha, K., and Levin, D., "Numerical Simulations of Atlas II Rocket Plumes," AIAA Paper 2001-0354, Jan. 2001.

[10]Isakovitz, S. J., *AIAA International Reference Guide to Space Launch System*, AIAA, Washington, DC, 1991.

[11]Wright, M. J., Rao, R. M., Candler, G. V., Hong, J. S., Schilling, T. S., and Levin, D. A., "Modeling Issues in the Computation of Plume Radiation Signatures," AIAA Paper 98-3622, July 1998.

[12]Ludwig, C. L., Malkmus, W., Reardon, J. E., and Thomson, J. A. L., *Handbook of Infrared Radiation from Combustion Gases*, NASA SP-3080, 1973.